Research in Astronomy and Astrophysics, 24:065007 (13pp), 2024 June https://doi.org/10.1088/1674-4527/ad3c6f

Inelastic Scattering of Dark Matter with Heavy Cosmic Rays

Keyu Lu[1], Yue-Lin Sming Tsai[2,3], Qiang Yuan[2,3], and Le Zhang[1,4,5]
[1] School of Physics and Astronomy, Sun Yat-sen University, Zhuhai 519082, China; zhangle7@mail.sysu.edu.cn
[2] Key Laboratory of Dark Matter and Space Astronomy, Purple Mountain Observatory, Chinese Academy of Sciences, Nanjing 210023, China; smingtsai@pmo.ac.cn, yuanq@pmo.ac.cn
[3] School of Astronomy and Space Science, University of Science and Technology of China, Hefei 230026, China
[4] CSST Science Center for the Guangdong-Hong Kong-Macau Greater Bay Area, SYSU, Zhuhai 519082, China
[5] Peng Cheng Laboratory, Shenzhen 518000, China

Received 2023 December 10; revised 2024 March 13; accepted 2024 April 2; published 2024 May 20

Abstract

We investigate the impact of inelastic collisions between dark matter (DM) and heavy cosmic ray (CR) nuclei on CR propagation. We approximate the fragmentation cross-sections for DM-CR collisions using collider-measured proton-nuclei scattering cross-sections, allowing us to assess how these collisions affect the spectra of CR boron and carbon. We derive new CR spectra from DM-CR collisions by incorporating their cross-sections into the source terms and solving the diffusion equation for the complete network of reactions involved in generating secondary species. In a specific example with a coupling strength of $b_\chi = 0.1$ and a DM mass of $m_\chi = 0.1$ GeV, considering a simplified scenario where DM interacts exclusively with oxygen, a notable modification in the boron-to-carbon spectrum due to the DM-CR interaction is observed. Particularly, the peak within the spectrum, spanning from 0.1 to 10 GeV, experiences an enhancement of approximately 1.5 times. However, in a more realistic scenario where DM particles interact with all CRs, this peak can be amplified to twice its original value. Utilizing the latest data from AMS-02 and DAMPE on the boron-to-carbon ratio, we estimate a 95% upper limit for the effective inelastic cross-section of DM-proton as a function of DM mass. Our findings reveal that at $m_\chi \simeq 2$ MeV, the effective inelastic cross-section between DM and protons must be less than $\mathcal{O}(10^{-32})$ cm^2.

Key words: elementary particles – nuclear reactions – nucleosynthesis – abundances – scattering – astroparticle physics – (cosmology:) dark matter

1. Introduction

Dark matter (DM) constitutes the majority of the matter in the universe and is thought to form a halo around our Milky Way comprised of non-relativistic particles. However, DM has only been observed through its gravitational interactions with standard model matter, such as gravitational lensing (Clowe et al. 2006). To detect non-gravitational interactions, several methods have been developed, including DM direct detection (Akerib et al. 2019; Wang et al. 2020a; Aprile et al. 2020, 2022; Meng et al. 2021; Aalbers et al. 2023; Elor et al. 2023), DM indirect detection (Chen & Kamionkowski 2004; Zhang et al. 2006, 2007, 2009, 2010; Zhang & Sigl 2008; Atwood et al. 2009; Slatyer et al. 2009; Ackermann et al. 2015; Choi et al. 2015; Slatyer & Wu 2018; Tulin & Yu 2018; Yin 2019; Leane 2020; Pérez de los Heros 2020; Xiao et al. 2020; Jaeckel & Yin 2021; Abbasi et al. 2023; Shao et al. 2023), and accelerator detection (Aad et al. 2021; Tumasyan et al. 2021). Those instruments focus primarily on detecting DM with a mass heavier than the GeV scale. If DM particles are lighter than GeV, they can evade the direct detection detector energy threshold due to their non-relativistic velocity.

Cosmic Rays (CRs) are high-energy particles originating from various astrophysical sources. In the event of a collision between high-energy CR particles and DM particles, the energy transfer between the two can potentially accelerate DM particles to a higher energy range (Bringmann & Pospelov 2019; Cappiello & Beacom 2019; Ema et al. 2019; Guo et al. 2020b; Wang et al. 2020b, 2023; Ge et al. 2021; Xia et al. 2021; Cui et al. 2022; Feng et al. 2022; Maity & Laha 2022; Xia et al. 2022; Su et al. 2023a, 2023b; Bell et al. 2023; Herrera & Murase 2023; Nagao et al. 2023). Alternatively, such collisions may also produce an indirect signal through smashed CRs (Cyburt et al. 2002; Hooper & McDermott 2018; Beylin et al. 2019; Guo et al. 2020a; Plestid et al. 2020). Therefore, incorporating CR-DM collisions in our analysis can enable us to explore sub-GeV DM parameter space within the current sensitivity of current detectors.

Although the fragmentation of heavy nuclei is well-studied in CR physics, see e.g., Genolini et al. (2018), the mechanism of the inelastic scattering between DM and CR heavy nuclei is still unclear (Bell et al. 2021; Alvey et al. 2023; Ambrosone et al. 2023). Therefore, we make two hypotheses to derive the DM-nucleus inelastic interaction cross-section:

1. When considering two collisions DM-CR and proton-CR, if the same kinetic energy of DM and proton are observed in the CR rest frame, the final kinetic energy distributions of particles in DM-CR and proton-CR are identical.
2. The DM-CR cross-section $\sigma_{\chi\text{-CR}}$ and the proton-CR cross-section $\sigma_{p\text{-CR}}$ are related by a phenomenological constant factor b_χ, namely $b_\chi \equiv \sigma_{\chi\text{-CR}}/\sigma_{p\text{-CR}}$.

Thanks to the recent development of satellite telescopes such as AMS-02 (Aguilar et al. 2016) and DAMPE (Chang et al. 2017), the statistical uncertainties of CR fluxes, especially for those secondary particles, have significantly improved. In this context, CR secondary particles may provide a useful probe for detecting inelastic scattering between DM and CRs. In this work, we propose to identify the DM-inelastic scattering between DM and CR heavy nuclei from the carbon and boron measured by AMS02 (Aguilar et al. 2016) and DAMPE (Alemanno et al. 2022).

The systematic uncertainties, including the diffusion coefficients D_0 and heights of the diffusion zone Z_h may dilute the impact of the inelastic collisions between DM and heavy CR nuclei on the CR propagation. To figure out their impacts on the 95% upper limits of b_χ, we simulate the DM-induced CR spectra with the 1σ favored region of D_0 and Z_h given by Yuan et al. (2020), despite of uncertainty degeneracy. Our work reveals that when considering uncertainties, the upper limits of b_χ for dark matter masses greater than 10 MeV can be weakened by more than one order of magnitude. However, for DM masses lighter than 1 MeV, DM signal can only contribute to the high-energy spectrum where the experimental error bars are significantly larger than those in the low-energy spectrum. The upper limits of b_χ with $m_\chi \approx 0.1$ MeV can only be slightly altered if including D_0 and Z_h systematic uncertainties.

The remainder of this paper is organized as follows. At the beginning of Section 2, we introduce the standard framework for CR propagation and discuss the propagation equation incorporating the inelastic scattering between DM and CRs. Then, in Section 2.1, we calculate the χ-CRs inelastic scattering cross-section by utilizing currently available collider data. Subsequently, in Section 3, we simulate the energy spectra of carbon C, oxygen O, boron B, and boron-to-carbon ratio (B/C) for cosmic rays with different DM particle masses. We also evaluate the characteristic signals of χ–CRs interaction. In Section 3.4, we show the exclusion region of χ–CRs interaction with the DM mass range between 10^{-4} and 10^{2} GeV by fitting the boron-to-carbon ratio. Finally, we give a summary and draw conclusions in Section 4.

2. Cosmic Rays Propagation in the Presence of DM

It is known that charged CRs diffuse in a random magnetic field of the Milky Way and collide with the interstellar medium (ISM) gas. During the propagation of cosmic nuclei, the spallation of cosmic nuclei can take place due to the collision. CR particles gain or lose energy and fragment into secondary particles. Naively, DM can also collide with high-energy cosmic nuclei to smash nuclei. Hence, we can modify the diffusion equation of CRs in the Milky Way (Strong et al. 2007; Evoli et al. 2008) by including CRs-DM collisions as

$$\begin{aligned}
&\frac{\partial N_i(p, r, z)}{\partial t} - \nabla \cdot (D_{xx}\nabla - \boldsymbol{v}_c) N_i \\
&+ \frac{\partial}{\partial p}\left(\dot{p} - \frac{p}{3}\nabla \cdot \boldsymbol{v}_c\right) N_i - \frac{\partial}{\partial p} p^2 D_{pp} \frac{\partial}{\partial p}\frac{N_i}{p^2} \\
&= Q_i(p, r, z) + \sum_{k=\mathrm{DM,\,gas}} \left[\sum_{\mathcal{A}_j > \mathcal{A}_i} \Gamma_k^s(j \to i; T) - \frac{N_i}{\tau_k^{f,i}(T)}\right] \\
&- \frac{N_i}{\tau_i^r}.
\end{aligned} \tag{1}$$

Here, $N_i(p, r, z)$ refers to the differential number density of the ith atomic species of CRs per unit momentum interval, and it is a function of the particle momentum p and the position in cylindrical coordinates (r, z). The convection velocity and the momentum loss rate are represented by $\boldsymbol{v}_c$ and $\dot{p} \equiv dp/dt$, respectively. For the purposes of our analysis, we assume a spatially homogeneous diffusion coefficient D_{xx}, as described in Maurin et al. (2010),

$$D_{xx} = D_0 \beta^{\eta} (R/R_0)^{\delta}, \tag{2}$$

where a particle with charge Ze has the rigidity $R \equiv pc/Ze$ and D_0 is a normalization parameter. The velocity of the particle, represented by β, is measured in units of the speed of light c. The power index δ reflects the property of the ISM turbulence, and a value of $\delta = 1/3$ for a Kolmogorov spectrum of turbulence is taken. $\mathcal{R}_0 \equiv 4$ GV is a reference rigidity To improve the fit of the data, a phenomenological modification of the diffusion coefficient at low energies is introduced through the parameter η, as discussed in Di Bernardo et al. (2010).

The process of reaccelerating CRs during their propagation in the turbulent galactic magnetic field is described by the momentum diffusion term D_{pp}. As shown in Seo & Ptuskin (1994), the diffusion coefficient D_{pp} can be related to D_{xx} via

$$D_{pp} D_{xx} = \frac{4p^2 v_A^2}{3\delta(4 - \delta^2)(4 - \delta)}, \tag{3}$$

where v_A is the Alfvén speed.

On the right-hand side of Equation (1), we incorporate all the interaction terms between CRs and ISM gas, as well as between CRs and DM. Note that the CR source term, except for spallation, is contained within $Q_i(p, r, z)$. We parameterize the timescales for fragmentation and radioactive decay as τ^f and τ^r, respectively. The kinetic energy per nucleon is $T \equiv (E - m_A)/\mathcal{A}$ with the total energy of a nucleus E, mass number $\mathcal{A}$, and mass $m_A \simeq \mathcal{A} m_{\text{nucleon}}$. In the most general form, the CR fragmentation due to gas or DM ($k = \mathrm{DM}$, gas) can be written as

$$\frac{1}{\tau_k^{f,i}(T)} \equiv n_k \sigma_{k,i}(T) \beta^i(T) c, \tag{4}$$

where k runs over DM, Hydrogen (H), and Helium (He), while i indicates the ith CR atomic species. The CR-DM, CR-Hydrogen, and CR-Helium cross sections are counted as $\sigma_{k,i}$. The total interstellar hydrogen density is $n_{\mathrm{H}} = n_{\mathrm{H\,I}} + 2n_{\mathrm{H}_2} + n_{\mathrm{H\,II}}$ and $n_{\mathrm{He}} \simeq 0.11 n_{\mathrm{H}}$. In this work, we safely ignore the contribution of heavier elements of the gas as CR targets. This is a reduction term, thus a negative sign in front of the CR fragmentation term. On the other hand, the production of secondary CR i generated from heavier element j spallation can be described as

$$\mathrm{CR}\, j + k \to \mathrm{CR}\, i + k + \mathrm{etc.}, \tag{5}$$

and the total inelastic scattering rate summing over the atom number condition $\mathcal{A}_j > \mathcal{A}_i$ cases is

$$\sum_{\mathcal{A}_j > \mathcal{A}_i} \Gamma_k^s(j \to i; T) = c n_k \sum_{\mathcal{A}_j > \mathcal{A}_i} \int dT' \beta(T') N_j(T') \times \left[\frac{d\sigma_k}{dT}(j \to i; T, T') \right], \tag{6}$$

where T' is the kinetic energy of the heavier CR particle j. The differential cross section of CR $j - k$ inelastic scattering is $d\sigma_k / dT$. The calculations for $d\sigma_{k=\mathrm{H,\,He}}/dT$ has been included in the code `GALPROP` (Strong & Moskalenko 1998). In this study, we use `GALPROP` to perform numerical calculations for the propagation of CRs.

2.1. Collision Cross Section between CRs and DM

Owing to our poor understanding of DM-nucleon interactions, the most straightforward method to simulate the fragmentation cross sections for all χ-CRs inelastic collisions is to replicate the spectra of CRs and proton (p) inelastic collisions. This study is based on two assumptions:

(1) Once the equivalent incoming kinetic energy of χ and p is observed in the CR rest frame, the final particle kinetic energy distributions in χ-CRs and p-CR are identical.

(2) The cross section for χ-CRs can be obtained simply by scaling the cross section for p-CR through $\sigma_{\chi\text{-CR}} = b_\chi \cdot \sigma_{p\text{-CR}}$. Here b_χ is a phenomenological constant factor that accounts for the strength of interactions between DM particles and cosmic rays.

When the mass of the DM particle is lighter than that of the proton, the shifted spectrum lies below the binding energy. Therefore, we can set the binding energy (B) as the energy threshold by utilizing the Bethe–Weizsäcker semi-empirical mass formula (Weizsäcker 1935),

$$ {}^{\mathcal{A}}_{Z}B = a_v \mathcal{A} - a_s \mathcal{A}^{2/3} - a_c \frac{Z^2}{\mathcal{A}^{1/3}} - a_a \frac{(\mathcal{A} - 2Z)^2}{\mathcal{A}} + \mathrm{sign} \times a_p \frac{1}{\mathcal{A}^{1/2}}. \tag{7}$$

The variables $\mathcal{A}$ and Z represent, once again, the nucleon number and proton number, respectively. The coefficients a_v, a_s, a_c, a_a, and a_p correspond to the volume, surface, Coulomb, asymmetry, and pair terms, respectively, as described in Kirson (2008). The values used in this study are as follows from Benzaid et al. (2020): $a_v = 14.9297$ MeV, $a_s = 15.0580$ MeV, $a_c = 0.6615$ MeV, $a_a = 21.6091$ MeV, and $a_p = 10.1744$ MeV. The sign in front of a_p is positive for an odd number of $\mathcal{A}$ and negative for an even number.

Next, we determine the mapping of kinetic energy in the case where the mass of DM particles differs from that of protons, i.e., $m_\chi \neq m_p$. Specifically, we consider the kinetic energies of DM and protons, denoted as $T_\chi^{[0]}$ and $T_p^{[0]}$, respectively, in the rest frame of the CR nucleus. Furthermore, we examine the kinetic energies of the CR nucleus, denoted as $T_{\mathrm{CR}}^{[\chi-\mathrm{Lab}]}$ and $T_{\mathrm{CR}}^{[p-\mathrm{Lab}]}$, respectively in the lab frame of χ-CRs and p-CR. By using the four-momentum conservation and assuming the relationship $T_\chi^{[0]} = T_p^{[0]}$, we can derive the corresponding replacement,

$$T_{\mathrm{CR}}^{[p-\mathrm{Lab}]} \to \frac{m_\chi}{m_p} T_{\mathrm{CR}}^{[\chi-\mathrm{Lab}]}. \tag{8}$$

Hence, the inelastic scattering cross section of χ-CRs in Equations (4) and (6) can be expressed as follows:

$$\frac{d\sigma_{\chi-\mathrm{CR}}}{dT}\left(T = T_{\mathrm{CR}}^{[\chi-\mathrm{Lab}]}\right) = b_\chi \frac{d\sigma_{p-\mathrm{CR}}}{dT}\left(T = \frac{m_\chi}{m_p} T_{\mathrm{CR}}^{[\chi-\mathrm{Lab}]}\right). \tag{9}$$

We can obtain the χ-CRs differential cross section $d\sigma_{\chi\text{-CR}}/dT$ straightforwardly, by shifting the DM-proton differential cross section $d\sigma_{p\text{-CR}}/dT$ toward lower (in the case of $m_\chi > m_p$) or higher (in the case of $m_\chi < m_p$) energies.

2.2. Configuration of Source and Propagation Parameters

In the stationary limit, $\frac{\partial N_i}{\partial t} = 0$, we solve the propagation equation using the publicly available code `GALPROP` Strong & Moskalenko (1998). The boundary condition, $N_i(r, z = |L|) = 0$, is applied to simulate free particle escape at the Galactic boundaries. For illustrative purposes, we engage two benchmark propagation models, detailed in Table 1.

Model A is characterized by parameters that accurately predict the nuclear spectra, for oxygen, carbon, and boron, as observed by AMS-02 and Voyager-1. Additionally, to accommodate both AMS-02 and DAMPE observations, we refine the propagation model to include an extra break in the

Table 1
Fiducial Propagation Model Utilized in this Study

Model	A	B
Diffusion coefficient D_0 (10^{28} cm^2 s^{-1})	4.10	3.32
Diffusion coefficient rigidity index δ	0.477	0.60
Diffusion coefficient velocity index η	−1.51	−0.61
Gradient of convection velocity dV_c/dz (km s^{-1} kpc^{-1})	0.0	0.0
Alfvén speed v_A (km s^{-1})	⋯	22.4
Height of diffusion zone Z_h (kpc)	4.93	3.61
Extra reference rigidity $\mathcal{R}_h$ (GV)	⋯	212.5
Extra diffusion coefficient rigidity index δ_h	⋯	0.25
Injection spectral index ν_0	0.70	0.41
Injection spectral index ν_1	2.40	2.35
Injection spectral index ν_2	⋯	2.42
Reference injection rigidity1 $\mathcal{R}_{br,1}$ (GV)	1.31	1.02
Reference injection rigidity2 $\mathcal{R}_{br,2}$ (GV)	⋯	142.3
Solar modulation Φ (GV)	0.742	0.690

Note. Detailed parameter estimation for Model A is available in Yuan et al. (2017, 2020), from fitting to the AMS-02 data, and for Model B in Ma et al. (2023) after adding the DAMPE B/C data.

diffusion coefficient (Ma et al. 2023), suggesting a transition in the rigidity-dependence slope to δ_h for $\mathcal{R} > \mathcal{R}_h$ (Model B).

The primary CR source was described as $Q_i(p, r, z)$ in Equation (1), which can be rewritten as

$$Q_i(p, r, z) = f(r, z) q_i(p), \tag{10}$$

where $f(r, z)$ and q_i represent the spatial distribution and the injection spectrum of the CR nuclei source, respectively.

The nuclei injection spectrum is assumed to be a broken power-law function of rigidity

$$q(\mathcal{R}) = q_0 \mathcal{R}^{-\nu_0} \prod_{i=1}^{n} \left[1 + \left(\frac{\mathcal{R}}{\mathcal{R}_{\mathrm{br},i}}\right)^s\right]^{(\nu_{i-1}-\nu_i)/s}, \tag{11}$$

where ν_0 is the spectral index at the lowest energies, ν_{i-1} and ν_i are spectral indices below and above break rigidity $\mathcal{R}_{br,i}$, and s describes the smoothness of the break which was fixed to be $s = 2$ throughout this work. We take $n = 2$ for Model B, and $n = 1$ for Model A. The spatial distribution of the primary CR particles $f(r, z)$ is similar to that of supernova remnants (SNRs) as

$$f(r, z) = \left(\frac{r}{R_\odot}\right)^a \exp\left[-\frac{b(r - R_\odot)}{R_\odot}\right] \exp\left(-\frac{|z|}{z_s}\right), \tag{12}$$

where $R_\odot = 8.5$ kpc is the distance between the solar system and the Galactic center, and $z_s \approx 0.2$ kpc is the characteristic height of the Galactic disk. We choose the shape parameters $a = 1.25$ and $b = 3.56$ measured from Trotta et al. (2011) to match the Galactic diffuse γ-ray emission and the ratio of H_2 to CO.

In the case of χ–CRs interactions, the density profile of the Milky Way halo is adopted to be the Navarro–Frenk–White (NFW) distribution (Navarro et al. 1996), expressed as:

$$\rho_\chi(r) = \frac{\rho_s}{(r/r_s)(1 + r/r_s)^2}, \tag{13}$$

with $r_s = 20$ kpc and $\rho_s = 0.26$ GeV cm^{-3}, thus in agreement with the local density of $\rho = 0.3$ GeV cm^{-3} at $r = 8.5$ kpc.

3. Numerical Results and Discussion

Given the impact of interactions between DM and CRs on the spallation process of heavy elements, it is challenging to comprehensively analyze their collective collisions if considering all DM-CR interactions simultaneously. To address this issue, we introduce a simplified toy model in Section 3.1, where DM particles exclusively interact with oxygen. In this work, we fix the solar modulation to $\Phi = 0.742$ GV for Model A and 0.69 GV for Model B.[6] Subsequently, in Section 3.2, we present the complete scenario, followed by an examination of the systematic uncertainties from D_0 and Z_h on CR spectra in Section 3.3. Finally, we constrain the DM model parameters by employing the measured B/C ratio spectra from the AMS-02 (Aguilar et al. 2017, 2018) and DAMPE (Chang et al. 2017) in Section 3.4.

We find that the collision terms between CRs and DM particles in Equation (1) are directly proportional to the DM parameters $b_\chi \rho_\chi / m_\chi$. While b_χ and m_χ are subject to a parameter-degeneracy, the peak of the DM-CR cross-section is also determined by m_χ. To disentangle the scaling factor and kinematics in the collision terms, we introduce a phenomenological variable, b_χ / m_χ. This allows us to set a clear separation between the role played by each of these parameters.

In this study, we employ the chi-squared χ^2 minimization to evaluate the statistical strength and constrain the DM collisions. We include the B/C ratio data from AMS-02 and DAMPE, and the total χ^2 can be written as

$$\chi^2(D_0, Z_h, m_\chi, b_\chi) = \sum_{\text{exper.}} \sum_i \frac{1}{\sigma_i^2} (f_i^{\text{obs}} - f_i^{\text{pred}})^2. \tag{14}$$

For each energy bin i, the experimental error is given by σ_i, while the predictions and observations of B/C ratio are denoted as f_i^{pred} and f_i^{obs}. Summing two experiments, the total 80 data points of all measured B/C ratios are within the range $0.6\ \text{GeV} < E_k/n < 4\ \text{TeV}$.

3.1. A Toy Model: Only DM-Oxygen Collisions

In this subsection, we consider a toy model that *DM particles only interact with oxygen*. This toy model is useful in tracking

---

[6] Although the solar modulation effect could potentially distort certain spectral characteristics, particularly those in the lower energy range, we follow fix $\Phi_{\mathrm{A}} = 0.742$ GV for Model A (Yuan et al. 2020), and $\Phi_{\mathrm{B}} = 0.69$ GV for Model B (Ma et al. 2023).

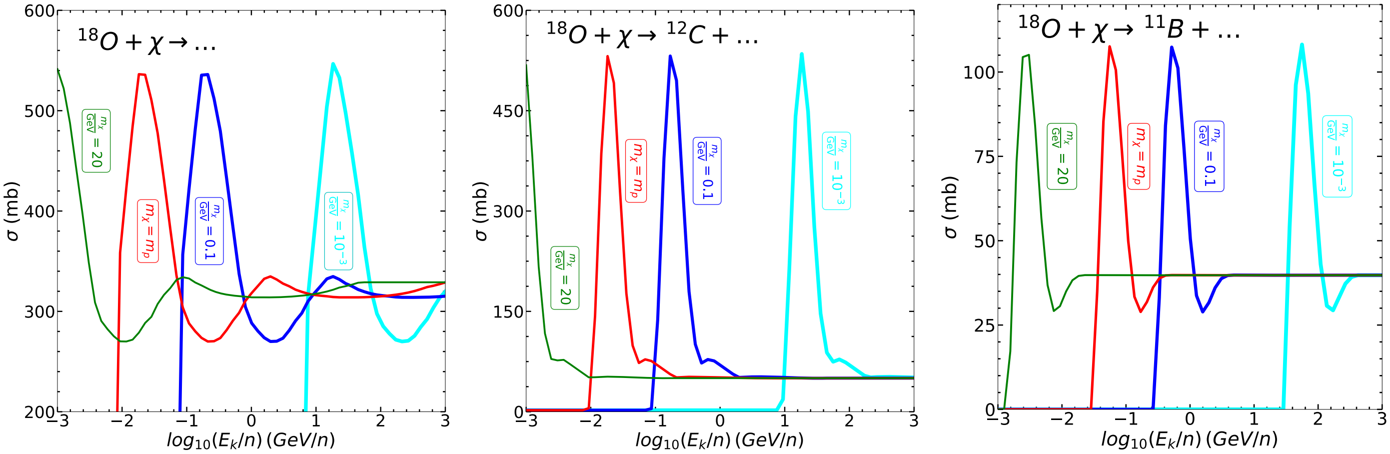

Figure 1. Comparison of the total cross-section for the fragmentation of oxygen into all feasible lighter nuclei (left panel) with the production cross-sections of carbon (middle panel) and boron (right panel), as a function of the kinetic energy per nucleon of ^{16}O. Four different DM benchmark masses $m_\chi=10^{-3}$ GeV, 0.1 GeV, m_p, 20 GeV are presented by cyan, blue, red, and green lines, respectively. The strength of DM-CRs interactions is fixed to be $b_\chi=1$.

the cascades of elements with $Z\leqslant 8$ produced by DM-oxygen collisions. The CR oxygen abundance can be depleted not only by collisions with protons but also by collisions with DM particles. The left panel of Figure 1 displays the dependence of the total cross-section for the fragmentation of oxygen into all possible lighter nuclei with respect to its kinetic energy per nucleon E_k/n. The production cross sections of carbon (via $^{16}\mathrm{O}+\chi\rightarrow{}^{12}\mathrm{C}+\cdots$) and boron (via $^{16}\mathrm{O}+\chi\rightarrow{}^{11}\mathrm{B}+\cdots$) are illustrated in the middle and right panels, respectively. To demonstrate the kinematics of the collisions between DM and CRs, we take four representative DM masses: two lines (cyan and blue) have DM mass lighter than gas particles (10^{-3} and 0.1 GeV), the red lines show the case $m_\chi=m_p$, and the green lines are with DM mass heavier than gas particles ($m_\chi=20$ GeV). By taking $b_\chi/m_\chi=1\,\mathrm{GeV}^{-1}$, the cross-section for $m_\chi=m_p$ case is exactly the same as the one for ^{16}O-proton collisions.

Based on Figure 1, our findings are summarized as follows.

1. The total fragmentation cross-section or the production cross-section of ^{10}B or ^{12}C exhibits a sharp peak.
2. If increasing m_χ, the peaks of the fragmentation and production cross sections shift to lower kinetic energy. This is because of the factor m_χ/m_p in Equation (8).
3. The ^{10}B production cross section is one order of magnitude lower than ^{12}C, thus the primary product of ^{16}O fragmentation is from carbon.

Next, we consider CR energy spectra by varying b_χ and m_χ for oxygen (Figure 2), carbon and boron (Figure 3), and the ratio of boron to carbon B/C (Figure 4). For propagation parameters, we use the values of Model A in Table 1. As adopted in Figure 1, we again show four different DM mass benchmarks, $m_\chi=10^{-3}$ GeV (cyan lines), $m_\chi=0.1$ GeV (blue lines), $m_\chi=m_p$ (red lines) and $m_\chi=20$ GeV (green lines). We present $b_\chi=0$ (black solid lines) for a DM-free scenario. When comparing the spectra based on different DM masses in these four left panels, we take $b_\chi/m_\chi=1\,\mathrm{GeV}^{-1}$ for a demonstration. In these right panels, we plot the spectra produced by CRs collision with 0.1 GeV DM, comparing with $b_\chi/m_\chi=1\,\mathrm{GeV}^{-1}$ and $b_\chi/m_\chi=0.1\,\mathrm{GeV}^{-1}$.

In the left panel of Figure 2, we can see the spectrum peak position and height slightly depending on the value of m_χ. Since we only consider the process $^{16}\mathrm{O}+\chi\rightarrow\cdots$ in this toy model, the total oxygen abundance can be reduced. Therefore, a larger fragmentation cross-section, as shown in Figure 1 can lower the total oxygen abundance. Because of the solar modulation and energy loss resulting from ionization and coulomb scattering within the $E_k\leqslant 1$ GeV region, the spectra of the three heavier scenarios differ from the DM-free scenario only by the height. Because we use $b_\chi/m_\chi=1\,\mathrm{GeV}^{-1}$ here instead of b_χ and m_χ, the heights of spectra are not too much different for various m_χ. In the case of $m_\chi=0.1$ GeV compared with the case that $m_\chi=m_p$, the flux peak shifts to the smaller energy $E_k\simeq 3$ GeV. For the heaviest mass case $m_\chi=20$ GeV, it is hard to find the difference to the $m_\chi=m_p$ case in the spectrum shape. Regarding the case with the lightest DM mass $m_\chi=10^{-3}$ GeV, the oxygen spectrum behaves like the one in a DM-free scenario at $E_k/n<5$ GeV, but a suppression happens at $E_k/n\geqslant 5$ GeV. Referring to the cyan lines in Figure 1, the highest peak of $m_\chi=10^{-3}$ GeV in the total fragmentation cross-section shifts to a higher E_k/n region, but that higher energy spectra are not solar-modulated. Therefore, we can see a suppression appears at $E_k/n\geqslant 5$ GeV.

In the right panel of Figure 2, we show the ^{16}O spectra by varying the size of b_χ/m_χ. As we expect, a larger b_χ/m_χ makes a large portion of ^{16}O being fragmented. However, the DM-

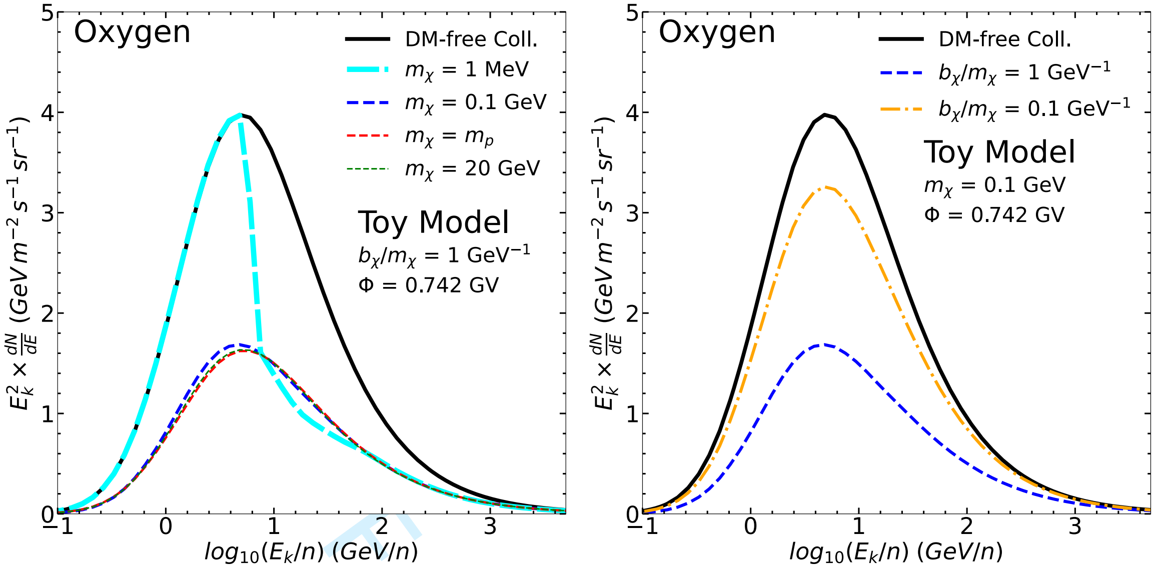

Figure 2. xygen energy spectra predicted by the DM-Oxygen toy model in a function of the kinetic energy per nucleon of ^{16}O, using the propagation parameters from Model A. The spectra are shown for four different DM masses, $m_\chi = 10^{-3}$ GeV (cyan), $m_\chi = 0.1$ GeV (blue), m_p (red), and 20 GeV (green), with $b_\chi/m_\chi = 1$ GeV^{-1} in the left panel. The right panel shows $b_\chi/m_\chi = 1$ GeV^{-1} (blue dashed line) and $b_\chi/m_\chi = 0.1$ GeV^{-1} (orange dashed–dotted line) for comparison. Both lines are based on $m_\chi = 0.1$ GeV. The black solid lines also give a spectrum for the DM-free scenario. Compared with the DM-free scenario, the fragmentation of oxygen due to the collision with DM leads to a decrease in the height of the spectrum.

oxygen collision can be polluted by proton-oxygen collisions so that the total decreasing amount of ^{16}O is not linearly proportional to the ratio b_χ/m_χ by comparing two cases $b_\chi/m_\chi = 1\,\mathrm{GeV}^{-1}$ (blue dashed line) and $b_\chi/m_\chi = 0.1\,\mathrm{GeV}^{-1}$ (orange dashed–dotted line).

In Figure 3, we show the boron and carbon spectra for varying m_χ (two left panels) and b_χ/m_χ (two right panels). Since the boron and carbon are mainly produced by oxygen fragmentation, the abundance of the boron and carbon can be enhanced if increasing b_χ/m_χ. Even if using the same b_χ/m_χ, only the lightest case $m_\chi = 10^{-3}$ GeV differs much from the other three masses due to the total fragmentation cross-section shifting to a higher E_k/n region.

In Figure 4, we show the B/C ratio as a function of the kinetic energy per nucleon by varying m_χ (left panel) or b_χ/m_χ (right panel). Interestingly, we notice that the B/C ratio spectrum appears to be more complex, particularly for the peaks of $m_\chi = 0.1$ GeV and $m_\chi = 10^{-3}$ GeV cases (blue and cyan dashed lines). Again, we have learned from Figure 1 that a DM particle with a mass lighter than the proton mass can shift the peak of the fragmentation cross-section toward the higher E_k/n region. On the other hand, a heavier DM particle ($m_\chi > m_p$) colliding with ^{16}O can shift the fragmentation cross-section peak to a lower E_k/n region so that the cross-section at the higher E_k/n region remains only half of the cross-section at the peak. Namely, the spectrum distortion for $m_\chi < m_p$ can be easier identified than the $m_\chi > m_p$ case. Moreover, we see from Figure 3 that the distortion in the carbon spectra can be stronger than the distortion in the Born spectra. Hence, the distortion in the B/C ratio spectra for $m_\chi < m_p$ case can be even more measurable than $m_\chi > m_p$ if b_χ/m_χ is large. When decreasing b_χ/m_χ as shown in the right panel of Figure 4, the distortion can be alleviated as expected.

3.2. The CR Spectra Including Full DM-CRs Collisions

In this subsection, we move to a general case that DM can collide with all the CR particles, from hydrogen ($Z = 1$) to nickel ($Z = 28$). Apparently, the cascade and fragmentation processes after DM-CR collisions become complicated and hard to backtrack precisely. The origins of the spectrum growth or reduction can be already washed out. Fortunately, the peak of the CR spectra still has some similarities with the toy model (DM-oxygen collision only) demonstrated in Section 3.1. Hence, we will only focus on the spectra of carbon, boron, and the B/C ratio.

Unlike the toy model presented in Figure 3, carbon spectra in two lower panels of Figure 5 are smaller than the spectra without DM-CRs collisions, even if using $b_\chi/m_\chi = 0.1\,\mathrm{GeV}^{-1}$ (the orange dashed–dotted line in the lower right panel). We find that the DM-carbon fragmentation cross-section is almost twice higher than the production cross-section of the $\chi + O \to C$ process, especially for the region with E_k/n higher than peak energy. On the other hand, carbon and oxygen abundance in the cosmic ray are comparable. Hence, the DM-induced spallation rate is faster for the carbon case than the DM-induced production rate. In the boron case, the CR boron

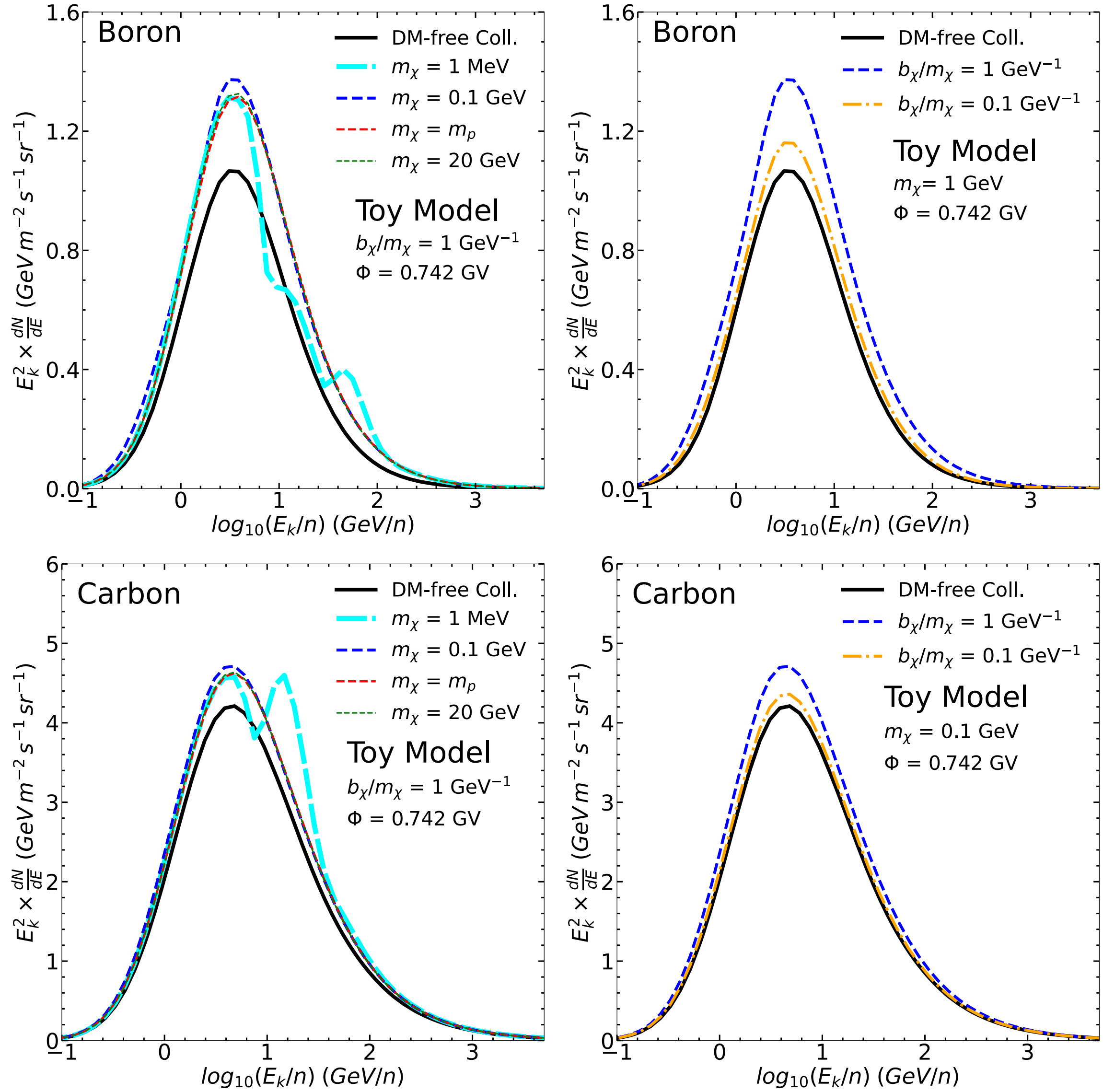

Figure 3. Boron (upper panels) and carbon (lower panels) energy spectra predicted by the DM-oxygen toy model in a function of the kinetic energy per nucleon of ^{10}B, using the propagation parameters from Model A. The color scheme is identical to that in Figure 2.

abundance is lower than the CR carbon abundance, but the cross-sections of boron produced by oxygen and carbon are higher than the boron fragmentation cross-section. Once a smaller boron fragmentation cross-section is applied, like the orange dashed–dotted line in the upper right panel, the boron production is sufficient to enhance the boron spectrum to be higher than the DM-free scenario.

In Figure 6, we plot the B/C ratio by including all DM-CRs collisions. In the left panel, we again compare four benchmark DM masses. Overall speaking, the spectrum shapes are similar to Figure 4, but the enhancement for $m_\chi = m_p$ case at the $E_k/n < 1$ GeV region is due to the cascade contributions from other heavier element fragmentation. Again, the peak feature of the green line ($m_\chi = 20$ GeV) is smeared out because of the solar modulation. However, the DM-induced peaks still appear in the light DM cases. Compared with Figure 4, the B/C ratios in the right panel of Figure 6 are generally greater, owing to the fact that the boron spectrum with the full DM-CRs collisions is higher than the carbon one as shown in Figure 5. Even if taking $b_\chi/m_\chi = 0.1\,\mathrm{GeV}^{-1}$, we can still clearly distinguish the DM-induced B/C ratio from the one without DM contribution.

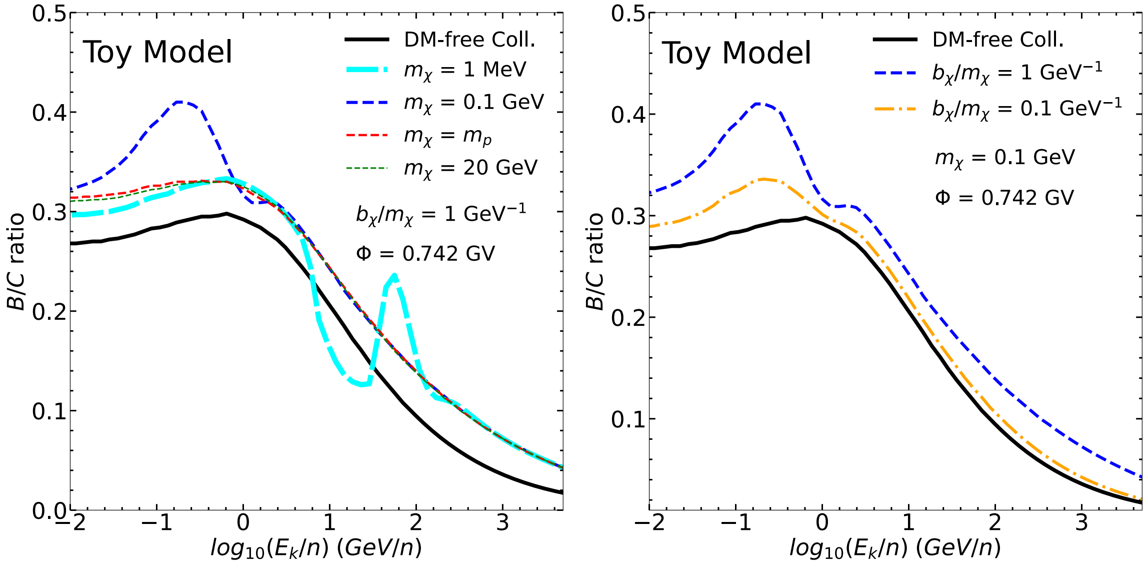

Figure 4. The B/C ratio as a function of the kinetic energy per nucleon, using the propagation parameters from Model A. The color scheme is identical to that in Figure 2.

3.3. Impacts of D_0 *and* Z_h *on the B/C Ratio*

The undetermined propagation parameters, such as D_0 and Z_h may introduce additional uncertainties. Thus, the DM-induced distortion of the B/C ratio becomes difficult to distinguish from the propagation uncertainties. For simplicity, we analyze the impacts using the one sigma regions of the diffusion coefficient ($D_0/(10^{28}\,\mathrm{cm}^2\,\mathrm{s}^{-1}) = 4.10 \pm 0.34$) and the semi-height of the diffusive zone ($Z_h/\mathrm{kpc} = 4.93 \pm 0.53$) from Model A (Yuan et al. 2017, 2020) For Model B, the values are $D_0/(10^{28}\,\mathrm{cm}^2\,\mathrm{s}^{-1}) = 3.32 \pm 0.55$ and $Z_h/\mathrm{kpc} = 3.61 \pm 0.69$ (Ma et al. 2023), all consistent with the fitted value of the radioactive cosmic ray and radio data ($Z_h = 4.1^{+1.3}_{-0.8}$) within a confidence level of approximately 1σ (Weinrich et al. 2020). However, Ginzburg et al. (1980) shows that the CR propagation is sensitive to D_0 and Z_h, but two parameters degenerate. Instead of considering both D_0 and Z_h, we only demonstrate the impacts of D_0 variation on the DM-CRs collision-induced B/C ratio in this subsection.

From Figure 6, we find no sharp peak in the B/C ratio due to DM collisions for $m_\chi > m_p$, and their B/C ratio spectra can be only overall scaled. Hence, we only take $m_\chi \leqslant m_p$ as examples to investigate two different DM masses ($m_\chi = m_p$ and 1 MeV).

In Figure 7, we display the B/C ratio spectra for two different DM masses. The black solid lines depict the B/C spectra for scenarios with $b_\chi/m_\chi \approx 0.02$, using propagation parameters from Model A (upper panels) and Model B (lower panels). The green dashed lines (Model A) and blue dashed lines (Model B) represent the B/C spectra of DM-free scenarios. Additionally, the green and blue bands show the 1σ region of the D_0 value. It is worth noting that similar B/C ratio spectra are observed in Models A and B when m_χ is fixed.

When $m_\chi = m_p$, there is no sharp peak observed in the B/C ratio spectra. In the case of a lighter DM mass ($m_\chi = 1$ MeV), a gap appears at around $E_k/n \sim 200$ GeV, followed by a peak at $E_k/n > 400$ GeV, consistent with Figure 6. The upper edge of the blue band corresponds to $D_0 = 2.77 \times 10^{28}\,\mathrm{cm}^2\,\mathrm{s}^{-1}$ (-1σ region), while the lower edge corresponds to $D_0 = 3.87 \times 10^{28}\,\mathrm{cm}^2\,\mathrm{s}^{-1}$ ($+1\sigma$ region). For the green band, the upper and lower edges correspond to $D_0 = 3.76 \times 10^{28}\,\mathrm{cm}^2\,\mathrm{s}^{-1}$ and $4.44 \times 10^{28}\,\mathrm{cm}^2\,\mathrm{s}^{-1}$. We plot the red and black error bars as the 1σ region for AMS-02 (Aguilar et al. 2016) and DAMPE (Alemanno et al. 2022) measurements. Regardless of the propagation models, changing D_0 results in a similar variation in the B/C ratio spectrum.

3.4. Constraints on DM Parameters

We now proceed to estimate the 95% upper limits of the parameter b_χ by using the B/C data from AMS-02 and DAMPE. Our statistic strength $\delta\chi^2$ with the given parameters $\{D_0, Z_h, m_\chi, b_\chi\}$ is defined as

$$\begin{aligned}\delta\chi^2(D_0, Z_h, m_\chi, b_\chi) = {} & \chi^2_{\mathrm{DM}}(D_0, Z_h, m_\chi, b_\chi) \\ & -\chi^2_{\mathrm{Bkg}}(D_0, Z_h),\end{aligned} \tag{15}$$

where DM-induced $\chi^2_{\mathrm{DM}}(D_0, Z_h, m_\chi, b_\chi)$ and DM-free $\chi^2_{\mathrm{Bkg}}(D_0, Z_h)$ are calculated with the expression given in Equation (14). For one-sided 95% upper limit of DM-CR interaction strength $b_\chi^{95\%}$, we require $\delta\chi^2(D_0, Z_h, m_\chi, b_\chi^{95\%}) = 2.71$ by fixing D_0, Z_h, and m_χ.

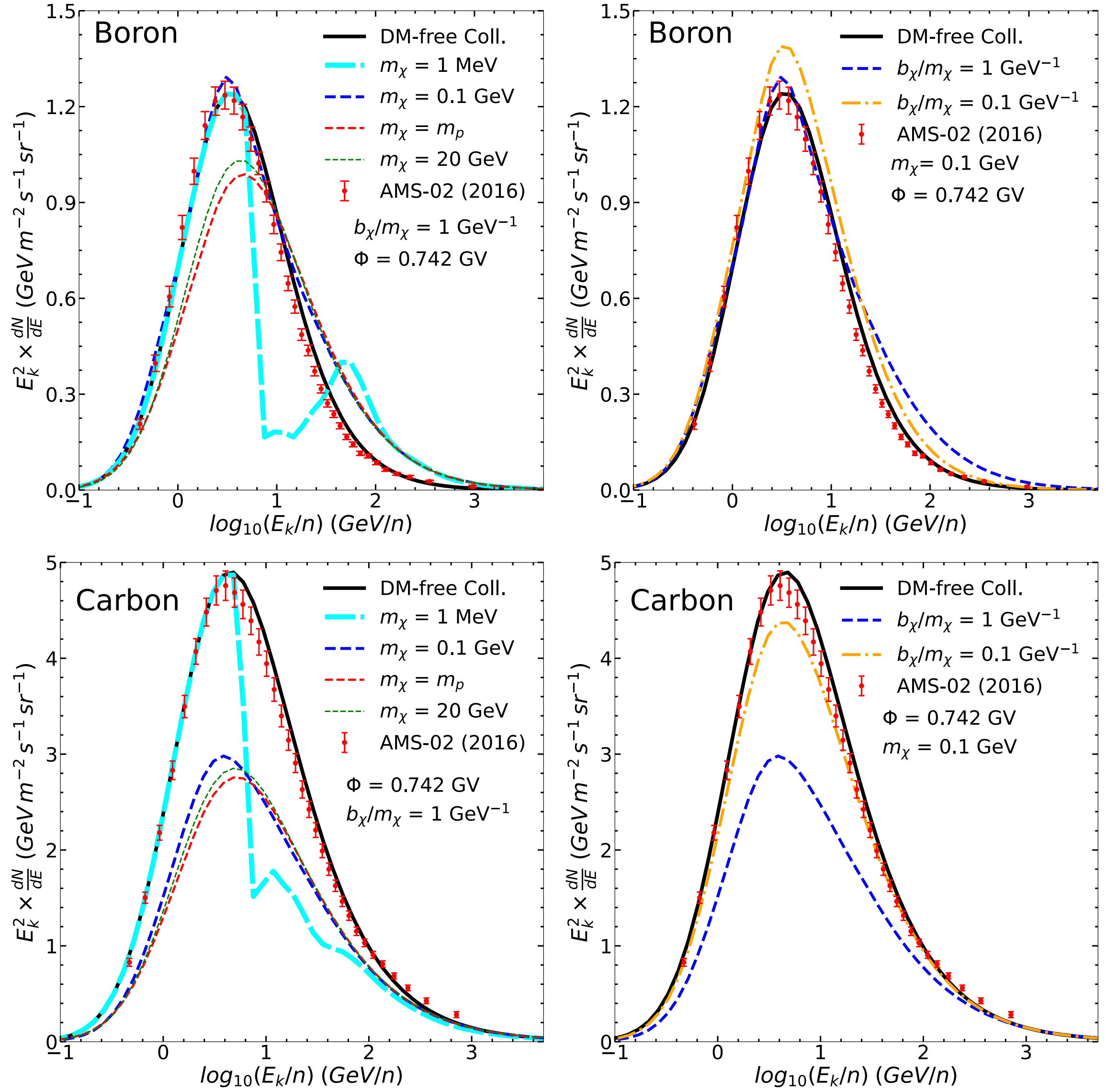

Figure 5. The energy spectra for boron (two upper panels) and carbon (two lower panels) with the propagation parameters given by Model A. The full interactions between DM and CRs are taken into account. The color scheme is the same as Figure 2, while the AMS-02 data are presented as red error bars. Two left panels show the spectra change with respect to m_χ, but the two right panels compare two different b_χ/m_χ by fixing m_χ.

In Figure 8, we present the 95% upper limit for the parameter b_χ, along with the 1σ uncertainty bands for parameters D_0 (left panel) and Z_h (right panel). The uncertainty bands derived from Model A are depicted in red, while those associated with Model B are shown in blue. In the context of a thermally produced DM scenario that involves a Dirac fermion DM and a complex scalar mediator, constraints from the Big Bang Nucleosynthesis (BBN) on $\Delta N_{\rm eff}$ establish a lower bound, suggesting that $m_\chi \leqslant 7.8\,{\rm MeV}$, as illustrated by the orange dashed lines (Krnjaic & McDermott 2020). For further reference, Table 1 lists the central values of the propagation parameters. Additionally, compared to Model A, Model B exhibits broader 1σ regions for both D_0 and Z_h, leading to the blue bands being wider than the red bands. We find three different behaviors in the 95% upper limits:

1. in the first mass region ($m_\chi > 0.1\,{\rm GeV}$), this region exhibits a trivial behavior because the B/C ratios are approximately proportional to Z_h/D_0. Hence, a larger Z_h or smaller D_0 requires a small value of b_χ to satisfy the AMS-02 and DAMPE B/C constraints.
2. in the second region ($2\,{\rm MeV} < m_\chi < 0.1\,{\rm GeV}$), we observe two distinct peaks in the B/C ratio spectrum

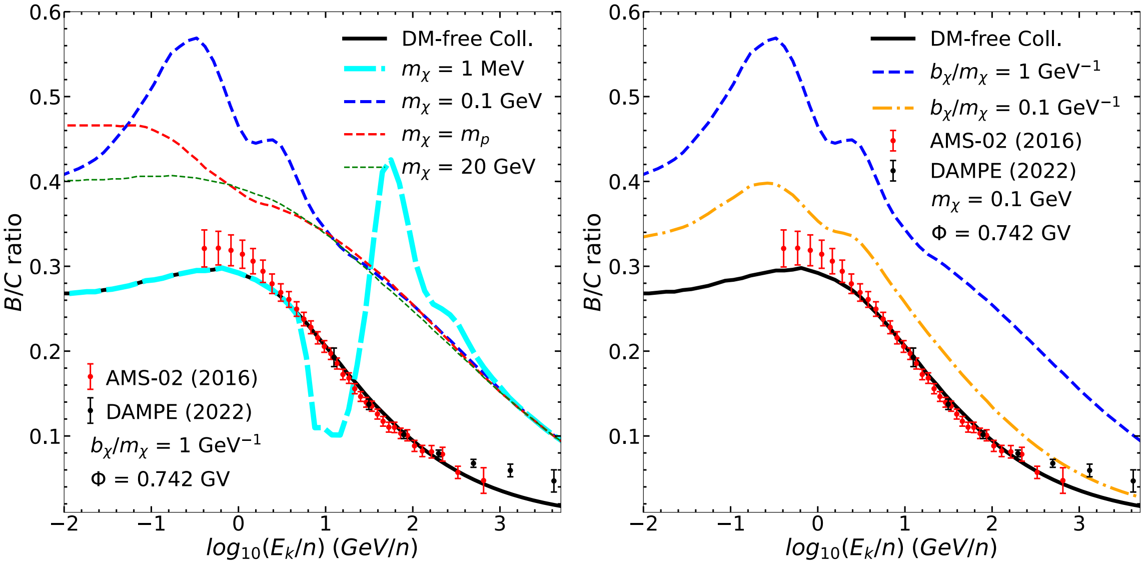

Figure 6. The B/C ratio similar to Figure 4 but for DM-CRs collisions fully implemented. The experimental data from AMS-02 and DAMPE are presented as red and black error bars.

due to DM-CRs collisions, as shown in Figure 6. These peaks of $2\,\mathrm{MeV} < m_\chi < 100\,\mathrm{MeV}$ shift to E_k/n around $\mathcal{O}(10^2)$ GeV, but the AMS-02 errors at the $10\,\mathrm{GeV} < E_k/n < 100\,\mathrm{GeV}$ region are relatively small. Furthermore, the systematic uncertainties induced by D_0 and Z_h are significantly reduced at $E_k/n > 10\,\mathrm{GeV}$. Consequently, as we decrease the value of m_χ within this mass range, the upper limits on b_χ become more stringent, while the systematic uncertainties gradually shrink.

3. in the third region ($m_\chi < 2\,\mathrm{MeV}$), when the values of m_χ are less than 2 MeV, the DM-induced peaks of the CR spectra enter the region with $E_k/n > 100\,\mathrm{GeV}$, where the error bars of AMS-02 and DAMPE measurements are the largest. On the other hand, the propagation uncertainties in this E_k region are significantly reduced. Therefore, unlike the other two mass regions, increasing the value of m_χ leads to more stringent limits on b_χ, with the impact of propagation uncertainties being relatively small. For $m_\chi < 100\,\mathrm{keV}$, the current B/C spectra measurements face challenges in probing DM-CR collisions, unless additional data points with $E_k/n > 3\,\mathrm{TeV}$ become available in the future.

Finally, we would like to examine the impact of Z_h/D_0 on the constraints imposed on b_χ. When we change either D_0 or Z_h within 1σ region, except for the $m_\chi < 2\,\mathrm{MeV}$ region, we observe that the 95% upper limits of b_χ are significantly altered, typically by around one order of magnitude. Furthermore, when combining the AMS-02 and DAMPE B/C ratio data in the region of small Z_h/D_0 uncertainties, we obtain $b_\chi < \mathcal{O}(10^{-7})$ for $m_\chi \simeq 2\,\mathrm{MeV}$.

4. Summary and Conclusions

Considering DM-CR inelastic scattering, the high-energy CRs can be smashed by plentiful non-relativistic DM particles. Such collisions can significantly alter the CR energy spectra whose shapes differ from the standard DM-free propagation. Thus, based on the successful CR propagation model and precise CR measurements, the interactions between DM-CRs can be constrained. In this work, we propose a model that DM-CR interaction mimics proton-CR interaction and a constant b_χ is used to scale all proton-CR inelastic collision cross-sections to the corresponding DM-CR inelastic collision cross-sections. By assuming that the final particle kinetic energy distributions in χ-CRs and p-CRs are identical when the incoming kinetic energy of χ and p is the same in the CR rest frame, we can study the CR spectra after DM-CR inelastic collisions.

We begin by exploring a simplified scenario using a toy model, where DM exclusively interacts with oxygen. The aim is to examine cascade productions resulting from DM-oxygen interactions. Our findings reveal that the B/C ratio spectrum remains unchanged for DM masses exceeding the proton mass ($m_\chi > m_p$). However, it might exhibit dual peaks for $m_\chi < m_p$. These patterns persist even when considering the full spectrum of DM-CR collisions, although tracing the cascade production in this more comprehensive scenario is more challenging. Focusing on a specific example with a coupling strength of $b_\chi = 0.1$ and a DM mass of $m_\chi = 0.1$ GeV, where DM interacts solely with oxygen, we observe a notable deviation

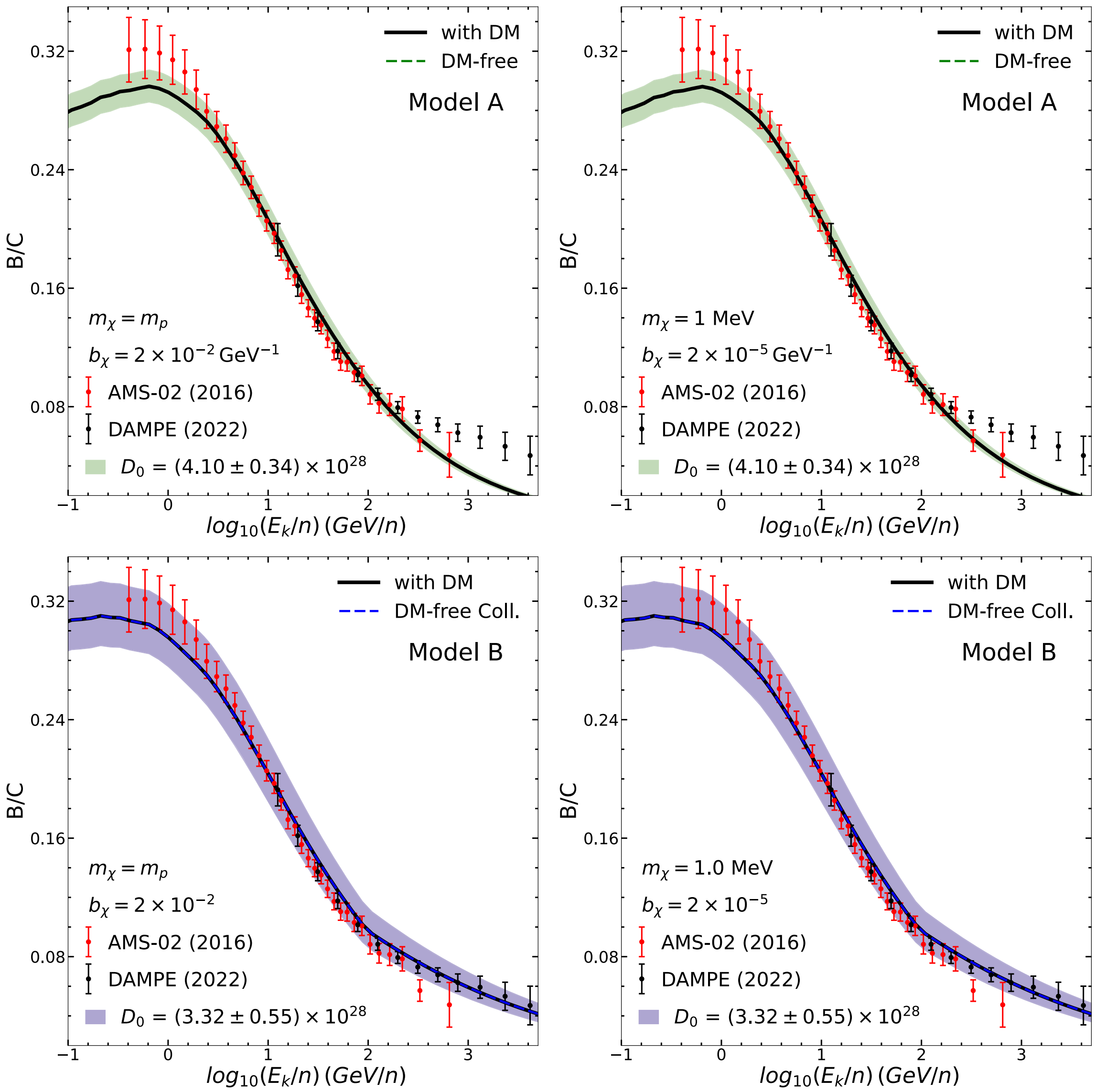

Figure 7. The B/C ratio spectra for two different masses, $m_\chi = m_p$ (left panels) and $m_\chi = 1$ MeV (right panels). The black solid lines depict the spectra with $b_\chi/m_\chi = 0.02$ using Model A (upper panels) and Model B (lower panels), while the dashed lines show spectra for the DM-free scenarios using Models A (green) and B (blue). The green and blue-shaded regions represent the DM-free scenarios by varying D_0 within the 1σ region from Model A and Model B, while the red and black error bars denote the 1σ of AMS-02 measurements (Aguilar et al. 2016) and the DAMPE measurements (Alemanno et al. 2022).

in the B/C spectrum due to the DM-CR interaction, a peak observed between 0.1 and 10 GeV experiences an enhancement of about 1.5 times. However, in a realistic model where DM collides with all CRs, this peak can be enhanced by up to twice its original value.

Once including the full DM-CRs collisions, we demonstrate the impact of propagation parameters D_0 and Z_h. By evaluating the Chi-squared from our predictions and measured B/C ratio spectra from AMS-02 and DAMPE, we find propagation uncertainties can degenerate with b_χ if $m_\chi > m_p$. However, it can be more tricky for $m_\chi < m_p$. Because the position of the peak in the B/C ratio varies from different DM particle masses, the peak shifts to higher energy regions if the DM mass gets lighter. In the DM mass region $0.1\,\mathrm{MeV} < m_\chi < 1\,\mathrm{MeV}$, the 95% upper limits of b_χ are less affected by propagation parameter Z_h/D_0. This is due to the fact that the DM-induced

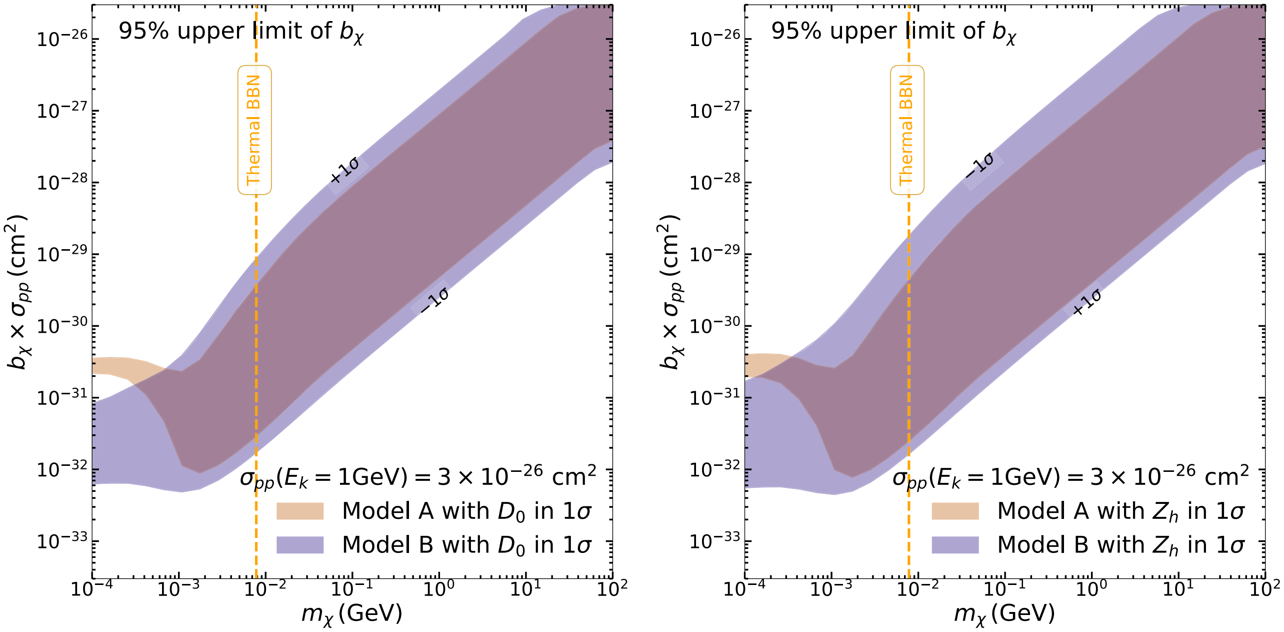

Figure 8. The 95% upper limit of b_χ. Instead of plotting b_χ in the y-axis, we show $b_\chi \times \sigma_{pp}$ to enable to cross-compare with proton-proton collision. The value $\sigma_{pp} = 3 \times 10^{-26}$ cm^2 is the proton-proton collision cross-section with $E_k = 1$ GeV. The upper and lower edges of the shaded regions represent the 1σ bounds for D_0 (left panel) and Z_h (right panel). The blue bands (Model A) present a 1σ range of $D_0/(10^{28}\ \mathrm{cm}^2\mathrm{s}^{-1}) = 4.10 \pm 0.34$ and $Z_h/\mathrm{kpc} = 4.93 \pm 0.53$, whereas the red bands (Model B) are defined by $D_0/(10^{28}\ \mathrm{cm}^2\mathrm{s}^{-1}) = 3.32 \pm 0.55$ and $Z_h/\mathrm{kpc} = 3.61 \pm 0.69$. For reference, the thermal BBN bound $m_\chi \leqslant 7.8$ MeV for a Dirac fermion DM is represented by an orange dashed line (Krnjaic & McDermott 2020).

spectrum peaks are located at $E_k/n > 100$ GeV region where the propagation uncertainties (see the blue shaded regions in Figure 7) are shrinking.

In summary, by combining the AMS-02 and DAMPE B/C ratio data, our result shows that b_χ will be less than $\mathcal{O}(10^{-7})$ if $m_\chi \simeq 2$ MeV, despite of a large propagation uncertainty $\mathcal{O}(10)$. For $m_\chi = 100$ keV, the propagation uncertainties are smaller, but the upper limit becomes $b_\chi < \mathcal{O}(10^{-5})$.

Acknowledgments

We thank Sujie Lin for discussing the `GALPROP` code. This work is supported by the National Key Research and Development Program of China (2022YFF0503304, 2020YFC2201600, 2018YFA0404504 and 2018YFA0404601), the Ministry of Science and Technology of China (2020SKA0110402, 2020SKA0110401 and 2020SKA0110100), the National Natural Science Foundation of China (11890691, 12205388 and 12220101003), the CAS Project for Young Scientists in Basic Research (YSBR-061, YSBR-092), the China Manned Space Project with No. CMS-CSST-2021 (A02, A03 and B01), the Major Key Project of PCL, and the 111 project (B20019).

ORCID iDs

Keyu Lu https://orcid.org/0000-0002-5828-3803
Le Zhang https://orcid.org/0009-0009-1374-7756

References

Aad, G., Abbott, B., Abbott, D. C., et al. 2021, JHEP, 11, 209
Aalbers, J., Akerib, D. S., Akerlof, C. W., et al. 2023, PhRvL, 131, 041002
Abbasi, R., Ackermann, M., Adams, J., et al. 2023, JCAP, 10, 003
Ackermann, M., Albert, A., Anderson, B., et al. 2015, PhRvL, 115, 231301
Aguilar, M., Ali Cavasonza, L., Ambrosi, G., et al. 2016, PhRvL, 117, 231102
Aguilar, M., Ali Cavasonza, L., Ambrosi, G., et al. 2017, PhRvL, 119, 251101
Aguilar, M., Ali Cavasonza, L., Ambrosi, G., et al. 2018, PhRvL, 120, 021101
Akerib, D. S., Alsum, S., Araújo, H. M., et al. 2019, PhRvL, 122, 131301
Alemanno, F., Altomare, C., An, Q., et al. 2022, SciBu, 67, 2162
Alvey, J., Bringmann, T., & Kolesova, H. 2023, JHEP, 01, 123
Ambrosone, A., Chianese, M., Fiorillo, D. F. G., Marinelli, A., & Miele, G. 2023, PhRvL, 131, 111003
Aprile, E., Aalbers, J,, Agostini, F., et al. 2020, JCAP, 11, 031
Aprile, E., Aalbers, J., Agostini, F., et al. 2022, PhRvL, 129, 161805
Atwood, W. B., Abdo, A. A., Ackermann, M., et al. 2009, ApJ, 697, 1071
Bell, N. F., Dent, J. B., Dutta, B., et al. 2021, PhRvD, 104, 076020
Bell, N. F., Newstead, J. L., & Shaukat-Ali, I. 2023, PhRvD, 109, 063034, arXiv:2309.11003
Benzaid, D., Bentridi, S., Kerraci, A., & Amrani, N. 2020, NuScT, 31, 9
Beylin, V., Bezuglov, M., Kuksa, V., Tretyakov, E., & Yagozinskaya, A. 2019, IJMPA, 34, 1950040
Bringmann, T., & Pospelov, M. 2019, PhRvL, 122, 171801
Cappiello, C. V., & Beacom, J. F. 2019, PhRvD, 100, 103011, [Erratum: Phys. Rev.D 104, 069901 (2021)]
Chang, J., Ambrosi, G., An, Q., et al. 2017, APh, 95, 6
Chen, X.-L., & Kamionkowski, M. 2004, PhRvD, 70, 043502
Choi, K., Abe, K., Haga, Y., et al. 2015, PhRvL, 114, 141301
Clowe, D., Bradac, M., Gonzalez, A. H., et al. 2006, ApJL, 648, L109
Cui, X., Abdukerim, A., Bo, Z., et al. 2022, PhRvL, 128, 171801
Cyburt, R. H., Fields, B. D., Pavlidou, V., & Wandelt, B. D. 2002, PhRvD, 65, 123503

Di Bernardo, G., Evoli, C., Gaggero, D., Grasso, D., & Maccione, L. 2010, APh, 34, 274
Elor, G., McGehee, R., & Pierce, A. 2023, PhRvL, 130, 031803
Ema, Y., Sala, F., & Sato, R. 2019, PhRvL, 122, 181802
Evoli, C., Gaggero, D., Grasso, D., & Maccione, L. 2008, JCAP, 10, 018, [Erratum: JCAP 04, E01 (2016)]
Feng, J.-C., Kang, X.-W., Lu, C.-T., Tsai, Y.-L. S., & Zhang, F.-S. 2022, JHEP, 04, 080
Ge, S.-F., Liu, J., Yuan, Q., & Zhou, N. 2021, PhRvL, 126, 091804
Genolini, Y., Maurin, D., Moskalenko, I. V., & Unger, M. 2018, PhRvC, 98, 034611
Ginzburg, V. L., Khazan, I. M., & Ptuskin, V. S. 1980, Ap&SS, 68, 295
Guo, G., Tsai, Y.-L. S., Wu, M.-R., & Yuan, Q. 2020a, PhRvD, 102, 103004
Guo, G., Tsai, Y.-L. S., & Wu, M.-R. 2020b, JCAP, 10, 049
Herrera, G., & Murase, K. 2023, arXiv:2307.09460
Hooper, D., & McDermott, S. D. 2018, PhRvD, 97, 115006
Jaeckel, J., & Yin, W. 2021, JCAP, 02, 044
Kirson, M. W. 2008, NuPhA, 798, 29
Krnjaic, G., & McDermott, S. D. 2020, PhRvD, 101, 123022
Leane, R. K. 2020, in Proc. of 3rd World Summit on Exploring the Dark Side of the Universe (EDSU2020), 203
Ma, P.-X., Xu, Z.-H., Yuan, Q., et al. 2023, FrP (Beijing), 18, 44301
Maity, T. N., & Laha, R. 2022, EPJC, 84, 1172
Maurin, D., Putze, A., & Derome, L. 2010, A&A, 516, A67
Meng, Y., Wang, Z., Tao, Y, et al. 2021, PhRvL, 127, 261802
Nagao, K. I., Higashino, S., Naka, T., & Miuchi, K. 2023, JCAP, 07, 061
Navarro, J. F., Frenk, C. S., & White, S. D. M. 1996, ApJ, 462, 563
Pérez de los Heros, C. 2020, Symm, 12, 1648
Plestid, R., Takhistov, V., Tsai, Y.-D., et al. 2020, PhRvD, 102, 115032
Seo, E. S., & Ptuskin, V. S. 1994, ApJ, 431, 705
Shao, Y., Xu, Y., Wang, Y., et al. 2023, NatAs, 7, 1116
Slatyer, T. R., Padmanabhan, N., & Finkbeiner, D. P. 2009, PhRvD, 80, 043526
Slatyer, T. R., & Wu, C.-L. 2018, PhRvD, 98, 023013
Strong, A. W., & Moskalenko, I. V. 1998, ApJ, 509, 212
Strong, A. W., Moskalenko, I. V., & Ptuskin, V. S. 2007, ARNPS, 57, 285
Su, L., Wu, L., Zhou, N., & Zhu, B. 2023a, PhRvD, 108, 035004
Su, L., Wu, L., & Zhu, B. 2023b, SCPMA, 67, 221012
Trotta, R., Jóhannesson, G., Moskalenko, I. V., et al. 2011, ApJ, 729, 106
Tulin, S., & Yu, H.-B. 2018, PhR, 730, 1
Tumasyan, A., Adam, W., Andrejkovic, J. W., et al. 2021, JHEP, 11, 153
Wang, Q., Abdukerim, A., Chen, W., et al. 2020a, ChPhC, 44, 125001
Wang, W., Wu, L., Yang, J. M., Zhou, H., & Zhu, B. 2020b, JHEP, 12, 072, [Erratum: JHEP 02, 052 (2021)]
Wang, W., Xu, W.-L., Yang, J. M., & Zhu, R. 2023, NuPhB, 995, 116348
Weinrich, N., Boudaud, M., Derome, L., et al. 2020, A&A, 639, A74
Weizsäcker, C. F. V. 1935, ZPhy, 96, 431
Xia, C., Xu, Y.-H., & Zhou, Y.-F. 2021, NuPhB, 969, 115470
Xia, C., Xu, Y.-H., & Zhou, Y.-F. 2022, JCAP, 02, 028
Xiao, L., Zhang, L., An, R., Feng, C., & Wang, B. 2020, JCAP, 01, 045
Yin, W. 2019, EPJWC, 208, 04003
Yuan, Q., Lin, S.-J., Fang, K., & Bi, X.-J. 2017, PhRvD, 95, 083007
Yuan, Q., Zhu, C.-R., Bi, X.-J., & Wei, D.-M. 2020, JCAP, 11, 027
Zhang, L., Chen, X., Kamionkowski, M., Si, Z.-g., & Zheng, Z. 2007, PhRvD, 76, 061301
Zhang, L., Chen, X.-L., Lei, Y.-A., & Si, Z.-g. 2006, PhRvD, 74, 103519
Zhang, L., Redondo, J., & Sigl, G. 2009, JCAP, 09, 012
Zhang, L., & Sigl, G. 2008, JCAP, 09, 027
Zhang, L., Weniger, C., Maccione, L., Redondo, J., & Sigl, G. 2010, JCAP, 06, 027